Characteristics of short-period wavelike features near 87 km altitude from airglow and lidar observations over Maui

J. H. Hecht,[1] A. Z. Liu,[2] R. L. Walterscheid,[1] S. J. Franke,[2] R. J. Rudy,[1] M. J. Taylor,[3] and P.-D. Pautet[3]

[1]   Small-scale (less than 15 km horizontal wavelength) wavelike structures known as ripples are a common occurrence in OH airglow images. Recent case studies attribute their origin to the presence of either convective or dynamical instabilities. However, little is known about their frequency of occurrence and period. The Maui-MALT Observatory, located at Mt. Haleakala, is instrumented with a Na wind/temperature lidar, which allows the determination of whether the atmosphere is dynamically or convectively unstable, and a fast OH airglow camera which takes images every 3 s with a sensitivity high enough to see the ripples. This study reports on 2 months of observations in October/November 2003 and in August 2004, eight nights of which also included Na lidar measurements. The imager results suggest that instability features occur in the 85- to 90-km region of the atmosphere for around 20% of the time. The nominal observed period for the ripples is between 2 and 4 min. While there are clear night-to-night variations, the average observed period is similar for both the 2003 and 2004 observations. In addition, a few of the small-scale structures are not ripples caused by instabilities but rather have features consistent with their being short horizontal wavelength evanescent waves. Their fractional intensity fluctuations are as large or larger than those of the ripple instabilities. Unlike the instabilities, the origin of the evanescent waves is not determined.

1.   Introduction

[2]   The advent of multi-instrumented ground-based observatories that make measurements of atmospheric characteristics from approximately 80 to 105 km altitude has allowed new studies of the dynamics of this region. Among the many interesting phenomena that have been characterized are a class of small-scale structures (generally less than 15 km horizontal wavelength) that appear in airglow imagers and have been called ripples. They were first described over 20 years ago by *Peterson* [1979] and have been further investigated by many groups [e.g., *Taylor and Hapgood*, 1990; *Taylor and Hill*, 1991; *Taylor et al.*, 1997; *Hecht et al.*, 1997; *Nakamura et al.*, 1999; *Hecht et al.*, 2000, 2001, 2004, 2005; *Li et al.*, 2005a, 2005b]. A recent review by *Hecht* [2004] suggested that many of these features are

caused by either dynamic instabilities, which originate from either large vertical wind shears or a combination of vertical wind shears and large negative vertical temperature gradients, or by convective instabilities which occur when superadiabatic temperature gradients are present.

[3]   Although the origin of these features is somewhat understood, the details of their generation are not well known. For example, they often appear as structures occupying only a small portion of the image, suggesting that atmospheric instabilities are quite localized. Furthermore, little is known of their temporal distribution. One of the reasons for this is that, as noted by *Hecht et al.* [2004], the observed period of a ripple event may be short (below 5 min). This short observed period is due to a typical ripple phase velocity near 50 m/s and a short horizontal wavelength which is often well below 15 km. The fractional fluctuation that ripples cause in the observed airglow intensity is also small. While many optical airglow imagers see ripples, few are optimized to study these features.

[4]   In addition to ripple structures, another class of short observed period wavelike features may be present in airglow images. Since the first mesopause region airglow imaging observations about 30 years ago [*Peterson and Kieffaber*, 1973], many of the observed structures have been attributed to the passage of internal atmospheric gravity waves (AGWs)

---
[1]Space Science Applications Laboratory, The Aerospace Corporation, Los Angeles, California, USA.

[2]Department of Electrical and Computer Engineering, University of Illinois, Urbana, Illinois, USA.

[3]Center for Atmospheric and Space Sciences, Utah State University, Logan, Utah, USA.

that are generated in the troposphere and propagate upward to the upper mesosphere and lower thermosphere [*Moreels and Herse*, 1977; *Hecht et al.*, 1995; *Swenson et al.*, 1995; *Taylor et al.*, 1995; *Nakamura et al.*, 1999; *Smith et al.*, 2000; *Ejiri et al.*, 2003; *Hecht*, 2004; *Pautet et al.*, 2005]. Internal AGWs have vertical phase variation and thus can freely propagate vertically. The observed periods of these waves are almost always longer than the Brunt-Vaisala period which is close to 5 min in the mesopause region. *Nakamura et al.* [1999] suggested that internal AGWs observed in OH images generally have horizontal wavelengths above 15 km.

[5] Internal acoustic waves, also characterized by having vertical phase variations, exist at very short intrinsic periods (the wave period in the frame of the background wind) always below the acoustic cutoff period that is generally about 4 min. Internal acoustic waves [*Beer*, 1974; *Gossard and Hooke*, 1975] are characterized by having phase speeds at or above the local speed of sound. (Because of these high phase speeds and relatively low background winds in the mesopause region the intrinsic and observed periods would be similar.) The exact period below which internal acoustic waves exist depends on the horizontal wavelength. For typical observed wavelengths near 30 km, this would be about a minute and a half.

[6] Evanescent or external waves are those with intrinsic periods between the upper limit of internal acoustic waves and the lower limit of internal AGWs. Such waves lack vertical phase variation and, thus, do not freely propagate vertically; instead, the wave amplitude decays away from the source altitude [*Walterscheid and Hecht*, 2003].

[7] To our knowledge, there are no definitive observations of internal acoustic waves in airglow images and few observations of evanescent waves [e.g., *Hecht et al.*, 2002]. The reason for this may be that, as for ripples, few imagers are designed to study such short-period features.

[8] In the past few years, a new imager had been deployed at Mt. Haleakala, Maui, as part of the Maui-MALT observatory [*Hecht et al.*, 2005; *Swenson*, 2005]. This imager operates in the near-IR part of the spectrum around 1.6 μm. In this region, the OH airglow signal is large, and integration times of 1 to 2 s result in a large signal to noise in an individual pixel. In routine operation, pixels are binned over approximately 20×20 km horizontal distances, assuming an 85- to 90-km altitude for the OH emission layer. When a time sequence of the OH emission intensity is plotted, it is noted that there are almost no wavelike features with observed periods below about 5 min even though images are produced every 3 s and, thus, the data are not limited by temporal resolution. However, when the bins are reduced to, say, 5×5 km, many features are observed with periods below 4 min. The small horizontal scale and the limited spatial and temporal extent of these features suggest that they may be ripple instabilities rather than acoustic or evanescent waves [e.g., *Hecht et al.*, 2004, 2005].

[9] To truly understand the nature of these features, however, auxiliary data are desirable. The Maui-MALT observatory includes a Na lidar capable of observing temperature. These data can be used to determine if there is any correlation between the observation of these features and atmospheric stability. Other instruments include a multiwavelength temperature mapper, which can record images in different altitudes, and a meteor radar which can   winds continuously.

[10] This study involves analyzing 2 months worth of imager data from clear periods in October/November 2003 and in August 2004. From these data, statistics are derived on the observed periods and occurrence frequency of the small-scale features. During this 2 months, there were eight nights of Na lidar data. Statistics from these data are used to calculate the probability of instability in the 85- to 90-km altitude region, the location of the bulk of the OH emission layer. These probabilities are compared to the occurrence of the ripples. During one particular period where a short observed period wave was seen, the nature of this wave, internal or evanescent, is determined.

2. Experimental Instrumentation and Technique

2.1. Instrumentation

2.1.1. Aerospace Near-IR Camera

[11] The Aerospace near-IR camera is described in some detail in the study of *Hecht et al.* [2005]. The camera, which is located near the summit of Mt. Haleakala, Maui (20.7°N, 156.3°W), combines a custom, wide-angle lens with a 256×256 HgCdTe detector array to provide images over an $\approx 73° \times 73°$ region of the sky. In an image, 128 pixels across the center is approximately equal to 40°, or 61 km, at 85 km altitude. The array consists of four 128×128 quadrants each with their own readout circuitry. Unfortunately, one 128×128-pixel quadrant has been lost. A fixed open filter position is used, allowing a spectral range $(1.55 - 1.7 \mu m)$ determined by the internal filters to be imaged. This spectral range is dominated by the OH Meinel airglow, and because the OH Meinel (4, 2) band brightness is almost 100 kRy, the signal to noise (S/N) for a 1-s integration is over 200:1. There is some geometric distortion in the images, especially near the edge of images, in that straight lines appear somewhat curved. Stars moving across the image from east to west move in somewhat curved lines away from the center pixels. The alignment of the imager with respect to geographic north and east is the same as was described in the paper of *Hecht et al.* [2005].

[12] Images are exposed for about 1.5 s, and images are obtained approximately every 3 s. For this work, data are taken in this mode for approximately 59.5 min each hour. For the last 30 s, a shutter is closed and dark images are taken. These dark images are typically about a factor of 30 or more less intense than the airglow image. They are not subtracted from the raw images.

[13] Table 1 provides a log of all the observations in October/November 2003 and in August 2004 when data were obtained.

2.1.2. UIUC Na Wind and Temperature Lidar

[14] The University of Illinois at Urbana-Champaign (UIUC) Na lidar was also described in the work of *Hecht et al.* [2005]. This lidar system uses a 3.67-m telescope and thus can measure winds and temperatures at better than 1-km vertical resolution with 90-s integration time. In normal operation mode, the lidar takes profiles in one of five positions: zenith (Z), 30° off zenith to the north (N), south (S), east (E), and west (W). Four of these positions are marked in Figure 1. Typically, these profiles are acquired in ZNEZSW sequence, and meridional or zonal winds are obtained by dividing the off-zenith line-of-sight wind by the sine of 30°. Temperatures are obtained from every profile.

Table 1. Observation Log

Date	Imager Time	Lidar Time
16 October 2003	0501–0855 UT	NA
18 October 2003	0800–0900 UT	NA
21 October 2003	0501–1300 UT	0823–1553 UT
22 October 2003	0501–1400 UT	NA
23 October 2003	0501–1459 UT	0751–1518 UT
25 October 2003	0601–1500 UT	NA
26 October 2003	0601–1500 UT	0439–1603 UT
27 October 2003	0500–1500 UT	NA
28 October 2003	0504–1500 UT	0519–1600 UT
1 November 2003	1001–1200 UT	NA
2 November 2003	1100–1400 UT	NA
3 November 2003	1201–1500 UT	NA
4 November 2003	1401–1500 UT	NA
5 November 2003	1301–1500 UT	NA
12 November 2003	0501–0600 UT	NA
13 November 2003	0500–0700 UT	NA
15 November 2003	0701–0900 UT	NA
2 August 2004	0601–0700 UT	NA
5 August 2004	0600–0900 UT	NA
6 August 2004	0600–0900 UT	NA
7 August 2004	0600–0900 UT	NA
9 August 2004	0601–1100 UT	0520–1534 UT
10 August 2004	0601–1200 UT	0615–1532 UT
11 August 2004	0601–1300 UT	0521–1535 UT
12 August 2004	0601–1400 UT	0540–1534 UT
13 August 2004	0601–1200 UT	NA
14 August 2004	0601–1500 UT	NA
15 August 2004	0601–1500 UT	NA
16 August 2004	0601–1500 UT	NA
17 August 2004	1201–1500 UT	NA
19 August 2004	0601–1500 UT	NA
20 August 2004	0701–1500 UT	NA
21 August 2004	0901–1500 UT	NA
22 August 2004	0801–1500 UT	NA
24 August 2004	1001–1500 UT	NA
25 August 2004	1101–1500 UT	NA

From these data, atmospheric stability parameters such as the Richardson number Ri can be obtained [*Hecht et al.*, 2005]. Note that the lidar data cover most but not all of the OH emission layer which typically peaks near 85 to 87 km but which can have some emission as low as around 80 km [*Hecht et al.*, 1998].

[15] Except where noted, all profiles are smoothed using a Hamming window with 1-km and 30-min full widths in altitude and in time, respectively. These smoothed profiles are interpolated onto a 15-min temporal and 100-m altitude grid. The effective full widths at half-maximum of this approach are about 0.5 km and 15 min, respectively.

[16] As noted in Table 1, lidar data were obtained on 21, 23, 26, and 28 October 2003 and on 9, 10, 11, and 12 August 2004. Most of these data are coincident or nearly coincident with the airglow observations. Exceptions to this are noted in section 3. The most significant exception occurred from about 8.5 to 10 UT hours on 10 August 2004 when the lidar was pointed in a fixed direction. This will be discussed later in detail.

2.1.3. UIUC Meteor Radar

[17] For part of the night on 10 August 2004, complete wind data are only available from the UIUC meteor radar also located in Maui but at the foot of Mt. Haleakala at 20.75°N, 156.43°W. This instrument is fully described in the study of *Franke et al.* [2005]. A single three-element Yagi antenna directed toward the zenith is used to illuminate

meteor trails. Meteor trail reflections are coherently detected on five three-element Yagi antennas oriented along two orthogonal baselines, with one antenna in the center of the array common to both baselines. On each baseline, the outer antennas are separated from the center antenna by 1.5 and 2.0 wavelengths. This configuration minimizes antenna coupling, provides enough redundancy to unambiguously determine the azimuth and elevation of most echoes, and provides excellent angular resolution for position determination.

[18] The standard format data sets are used in this analysis. This standard format provides hourly winds in the altitude range of 80–100 km, sampled every 1 km. The altitude resolution of these estimates is determined by a triangular weighting function with half-width of 3 km and base width of 6 km.

2.1.4. Utah State University Mesospheric Temperature Mapper

[19] To determine the vertical extent of wave activity during 10 August 2004, some data from the Utah State University Mesospheric Temperature Mapper (MTM) are also used. This instrument is described in the paper of *Taori et al.* [2005]. The MTM is a high-performance solid-state imaging system capable of observing wave-induced fluctuations in the intensity and rotational temperature of the OH (6, 2) Meinel band and the O2 (0, 1) Atmospheric band emissions.

2.2. Analysis Techniques

[20] Since the data used in this paper from the MTM and the meteor radar are quite limited, and are standard products, no special details of those analysis techniques are needed. The analysis of the lidar data is also to be found in the paper of *Hecht et al.* [2005]. It is reviewed briefly below. However, the analysis of the Aerospace camera data
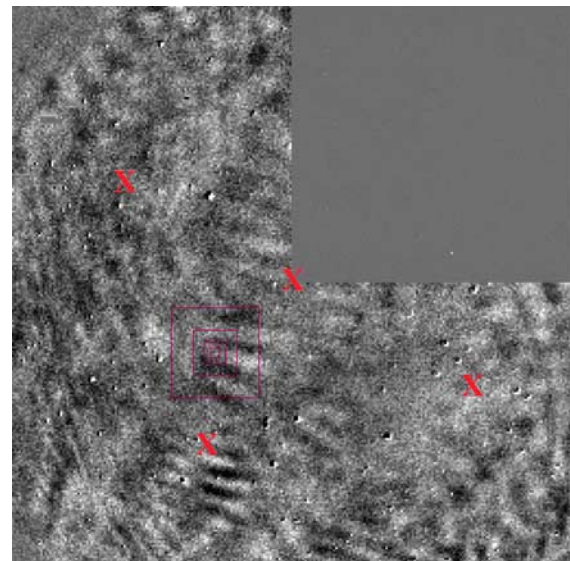
Figure 1. The difference between two OH images taken 1 min apart at 7.75 UT hours on 11 August 2004. The four red squares are in order of decreasing sizes: 40 × 40, 20 × 20, 10 × 10, and 4 × 4 pixels. The red X symbols mark the approximate positions of the lidar observations within the imager observation field.

is somewhat new and will be discussed in detail following the lidar discussion.

2.2.1. Lidar

[21] In this work, several parameters are shown which can indicate the presence of instabilities or evanescent waves. These have been discussed previously in the studies of *Beer* [1974], *Gossard and Hooke* [1975], and *Hecht et al.* [2002, 2005].

2.2.1.1. Richardson Number, *Ri*

[22] The stability of atmospheric regions is most easily quantified by the Richardson number, *Ri*, which is given by

$$Ri = \frac{N^2}{(\mathrm{d}U/\mathrm{d}z)^2} \tag{1a}$$

$$Ri = \frac{(g/T)(\mathrm{d}T/\mathrm{d}z + g/C_p)}{(\mathrm{d}U/\mathrm{d}z)^2} \tag{1b}$$

where N is the Brunt-Vaisala frequency and $\mathrm{d}U/\mathrm{d}z$ is the horizontal wind shear, the variation of the horizontal wind as a function of altitude, z. The square of N is given by the numerator of equation (1b), where T is the temperature, $\mathrm{d}T/\mathrm{d}z$ is the vertical temperature gradient, g is the gravitational acceleration, and C_p is the atmospheric specific heat at constant pressure. The quantity g/C_p is the adiabatic lapse rate which is typically about 10 K/km in the 85- to 90-km altitude region.

[23] There are two instability regimes which occur. When Ri is between 0 and 0.25, a dynamical instability is likely to occur which leads to the formation of Kelvin-Helmholtz (KH) billows. However, if N^2 is less than 0, which occurs when the atmospheric lapse rate exceeds the adiabatic lapse rate, a convective instability is likely to occur resulting in a different type of feature.

[24] Examples of KH features seen in OH images with coincident lidar data are shown in the studies of *Hecht et al.* [2005], *Li et al.* [2005a], and *Li et al.* [2005b]. Examples of convective features seen in OH images with coincident lidar data are shown in the papers of *Hecht et al.* [1997] and *Li et al.* [2005b].

2.2.1.2. Vertical Wave Number, *m*

[25] Consider an AGW at an altitude z above its source in an atmosphere where H is the atmospheric scale height. The vertical wave number, m, is given by $2\pi/\lambda_z$, where λ_z is the vertical wavelength. The vertical wave number obeys the following dispersion relation:

$$m^2 = (2\pi/\lambda_z)^2 = \frac{(N^2 - \omega_I^2)(k^2)}{(\omega_I^2 - f^2)} + \frac{\omega_I^2}{C^2} - \frac{1}{4H^2} \tag{2a}$$

$$m^2 = \frac{(N^2 - \omega_I^2)(k^2)}{(\omega_I^2 - f^2)} + \frac{(\omega_I^2 - \omega_a^2)}{C^2} \tag{2b}$$

In equation (2a), C is the speed of sound, ω_I is the intrinsic frequency with respect to a frame of reference that moves with the background wind, k is the horizontal wave number equal to $2\pi/\lambda_h$, and f is the inertial frequency which is $2\Omega \sin(\phi)$, where ϕ is latitude and Ω is the angular speed of

the Earth. For a given background wind velocity component, $\overline{u}$, in the direction of the wave, and an observed wave horizontal phase velocity, c, the Doppler-shifted wave phase velocity $(c\text{-}\overline{u})$ is equal to $(\omega_I)(\lambda_h)/(2\pi)$ or simply (λ_h/τ_I). The observed period is equal to λ_h divided by the observed phase velocity, c. The intrinsic period is equal to λ_h divided by the Doppler-shifted phase velocity. In equation (2b), the acoustic cutoff frequency, ω_a, is given by $C/(2H)$ in an isothermal atmosphere. In a nonisothermal atmosphere, the expression for ω_a is modified, and an extensive discussion of the implications of this is given in the work of *Walterscheid and Hecht* [2003].

[26] The vertical wave number, m, thus depends on the background wind, the background temperature, and the vertical temperature gradient. When the wind and temperature profiles are such that m is real, the AGW is internal and thus is freely propagating vertically. However, if m is imaginary, then the wave is evanescent and there is no vertical phase progression. Since internal AGWs always have intrinsic periods above the Brunt-Vaisala period, which is obtained, from the inverse of the Brunt-Vaisala frequency, waves with intrinsic periods below that may be evanescent. This period is typically around 5 min at altitudes around 85 to 90 km but depends on the temperature gradient. As the intrinsic period decreases eventually, the internal acoustic wave regime will occur. The exact period for this depends on the horizontal wavelength of the wave. The phase velocity for internal acoustic waves is at or above C. More details on this are given in the paper of *Walterscheid and Hecht* [2003]. Except where noted, references to a measured wave period are to the observed period.

2.2.2. Aerospace Near-IR Camera

2.2.2.1. Time Series Plots

[27] Raw images obtained from this camera have been shown in the study of *Hecht et al.* [2005]. As noted in that work, ripples and wavelike features are often more easily visible when difference images are shown. Figure 1 shows such an image which is the difference between two images taken 1 min apart at 7.75 UT hours on 11 August 2004. The small white round features, always dark on the left, are stars that have moved about 1 pixel in a minute. Wavelike features, similar to the dynamic Kelvin-Helmhotz instability discussed in the work of *Hecht et al.* [2005], are visible in the center of the image.

[28] Although some individual images are discussed in this work, most of the analysis is concerned with time series of the OH intensity fluctuations. In Figure 1, four red boxes are shown. Their sizes are 40×40, 20×20, 10×10, and 4×4 pixels. These will be referred to as either the 40-, 20-, 10-, or 4-pixel smoothing. The center of the smallest square is 93 pixels from the two nearest edges. Since a pixel is approximately 0.5 km, these are approximately equivalent to 20×20, 10×10, 5×5, and 2×2 km squares. To obtain a time series plot, the average intensity in each square is reported. However, all such time series are obtained from the raw images, not from the difference images. In each raw image, the boxes are at the same fixed location as shown in the Figure 1 difference image.

[29] Time series of OH emission intensities, obtained approximately (within 10%) every 3 s, are shown in Figure 2a from 6 to 13 UT hours on 11 August 2003. Here the 30 s, when dark images were obtained at the end of each hour, has
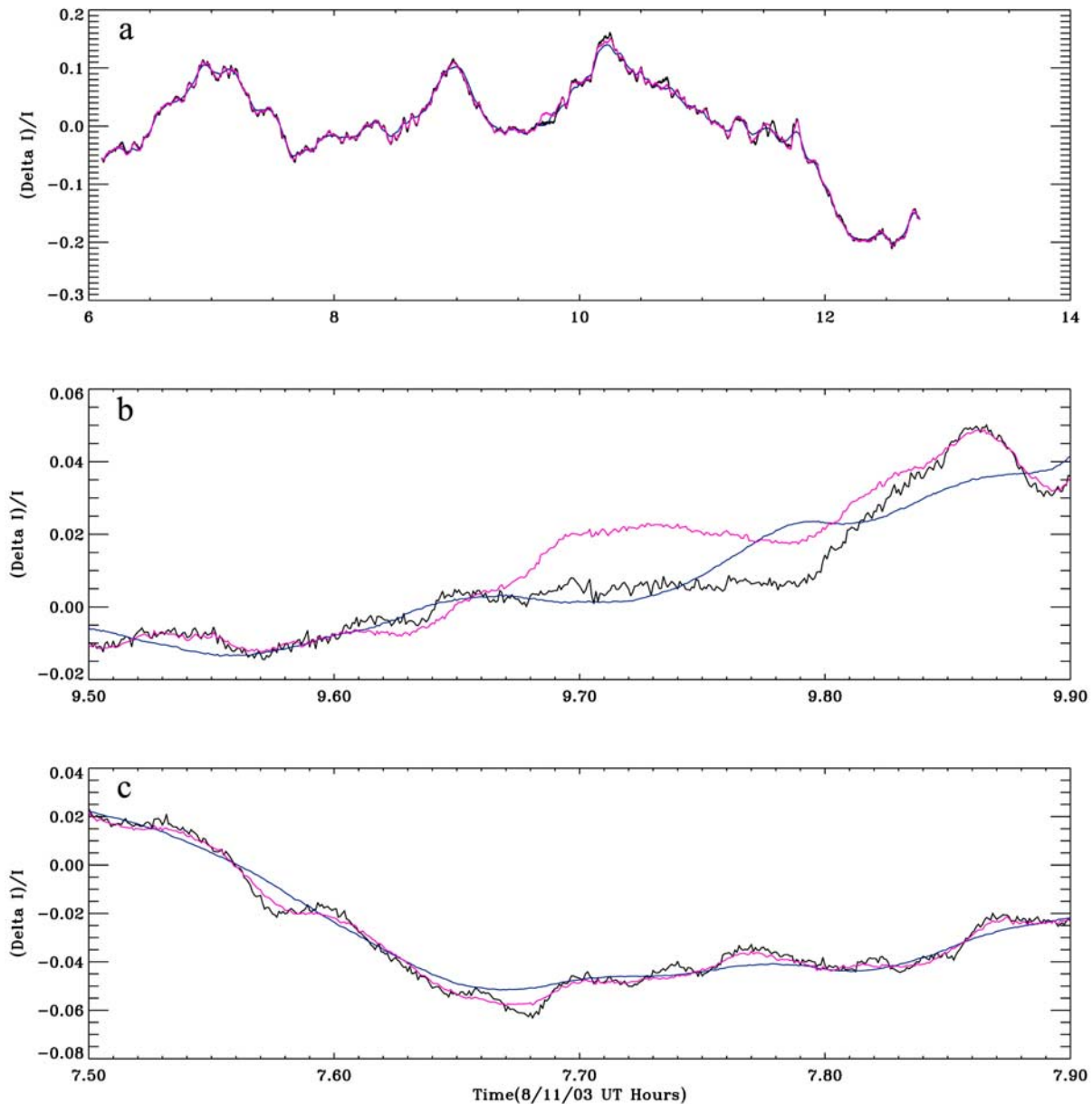
Figure 2. Plots of the fractional fluctuation of the OH intensity on 11 August 2003 measured as a function of time using the designated squares. In these panels, the black line uses the 4-pixel smoothing, the red line, which falls almost on top of the black line, uses the 10-pixel smoothing, and the blue line uses the 40-pixel smoothing. (a) 6–13 UT hours. (b) 9.5–9.9 UT hours. (c) 7.5–7.9 UT hours.

been linearly interpolated, and the time series have been interpolated onto a time grid sampled exactly every 3 s. In this plot, the mean intensity has been subtracted, and the resultant data have been divided by this mean. Figure 2a shows the resultant OH intensity fluctuation plot as a function of time. In this panel, the black line uses the 4-pixel smoothing, the red line, which falls almost on top of the black line, uses the 10-pixel smoothing, and the blue line uses the 40-pixel smoothing. Note that for the 40-pixel smoothing, most of the short (below 4 min) period fluctuations are eliminated.

[30] There are several phenomena that can cause fluctuations in these time series. The first is stars passing through the box. Related to th   uld be blobs of enhanced or depressed OH intensity passing through the box. A second would be wavelike fluctuations such as the features seen in Figure 1.

[31] Figure 2b shows an example of a star passing through the 10 × 10-pixel box around 9.7 UT hours. As can be seen in Figure 1, an individual star occupies only a few pixels, and in this case, the star did not pass through the 4 × 4-pixel box. Thus the red line plot shows an increase in signal but the black line plot does not. There is also no obvious response in the blue line 40 × 40-pixel plot. The reason for that is that the star is small compared to the box size, so that the 0.02 fluctuation seen in the 10 × 10-pixel box is reduced by a factor of 16 in the larger box. Fluctuations due to stars
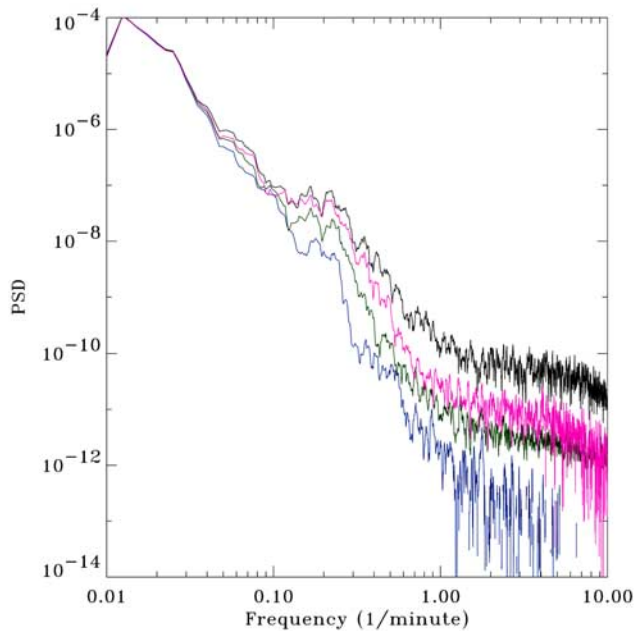
Figure 3. Plot of the power spectral density (PSD) of a slightly modified version of the time series shown in Figure 2a. A linear slope has been taken out so the beginning and end points are the same. The colors correspond to those in Figure 2a except that the 20×20-pixel smoothed plot, not shown there, has also been analyzed and is shown in green.
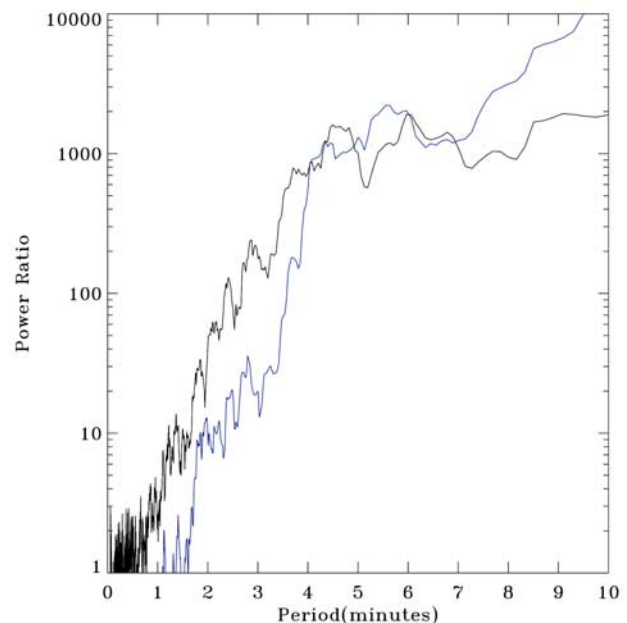
2.2.2.2. Fourier Spectral Analysis

[34] Figure 3 shows the power spectral density (PSD) of a slightly modified version of the plots in Figure 2a obtained from taking a windowed Fourier transform. Before applying the transform, a linear trend has been removed from the time series in Figure 2a. The colors correspond to those in Figure 2a except that the 20×20-pixel plot, not shown there, has also been analyzed. What is especially apparent is that just for frequencies above about 0.2 per minute, the 40×40-pixel data show a sharp drop in power not seen in the 4- or 10-pixel smoothing.

[35] Figure 4 shows two line plots of the signal to noise of the PSD. The black line shows the ratio of the PSD to the noise, for the 4-pixel smoothing, where the noise level is that measured at a frequency near 5 per minute. The blue line shows the same ratio, for the 40-pixel smoothing, scaled upward by a factor, so that the two plots are about the same at a period of 4 min for the purposes of the following comparison. Note the excess power between 1 and 4 min for the 4-pixel smoothing. The excess power between 1 and 4 min is consistent with what was discussed in the previous section where it was stated that few waves with periods below 4 min were seen in the 40-pixel smoothed plots. (As can be seen from Figure 3 the excess power for the 40-pixel smoothed plot at periods above 7 min is a consequence of the arbitrary scaling applied for Figure 4.)

2.2.2.3. Wavelet Analysis

[36] A main objective of this study is to determine the frequency of occurrence of short-period waves. Fourier transforms are not localized in time and thus are not well

are rarely seen in the time plots for several reasons. As can be seen in Figure 1, only a few bright stars will pass through the boxes during the night as the motion of the stars is 15° per hour and that there are only a few stars bright enough to be seen in these plots. Furthermore, because of this slow motion, they are easily distinguished from other more common phenomena since the period will scale with box size. So even if a star only passes through a corner of the 4-pixel box in 2 min, it will appear to traverse the 10-pixel box in a much longer time. As can be seen in Figure 2b, and as is true for most of the data, the short-period fluctuations have very similar periods in both the 4- and 10-pixel smoothed plots.

[32] Blobs of enhanced or depressed OH emission will appear similar to stars. If the size of the blobs is small compared to the box, then the period will vary depending on the size of the box. Blobs that are large compared to the size of the box will appear flat-topped in the time series. The intensity will rise rapidly and then will appear constant as the blob passes through.

[33] Figure 2c shows the time series with the most common situation when a wavelike feature such as seen in Figure 1 passes through a box. In Figure 1, it is easy to see that the scale size of the feature is around 20 pixels (10 km), and thus it should be present with similar periods in the 4- and 10-pixel plots but be suppressed in intensity in the 40-pixel plot. That is indeed what is seen. Note that the blue line plot appears to be the average intensity of the background after the wavelike features are smoothed. The red line and black line plots are both abo   below the blue line.

Figure 4. Two line plots of the signal to noise of the PSD. The black line shows the ratio of the PSD to the noise, for the 4-pixel smoothing, where the noise level is that measured at a frequency near 5 per minute in Figure 3. The blue line shows the same ratio, for the 40-pixel smoothing, scaled upward by a factor, so that the two plots are about the same at a period of 4 min.
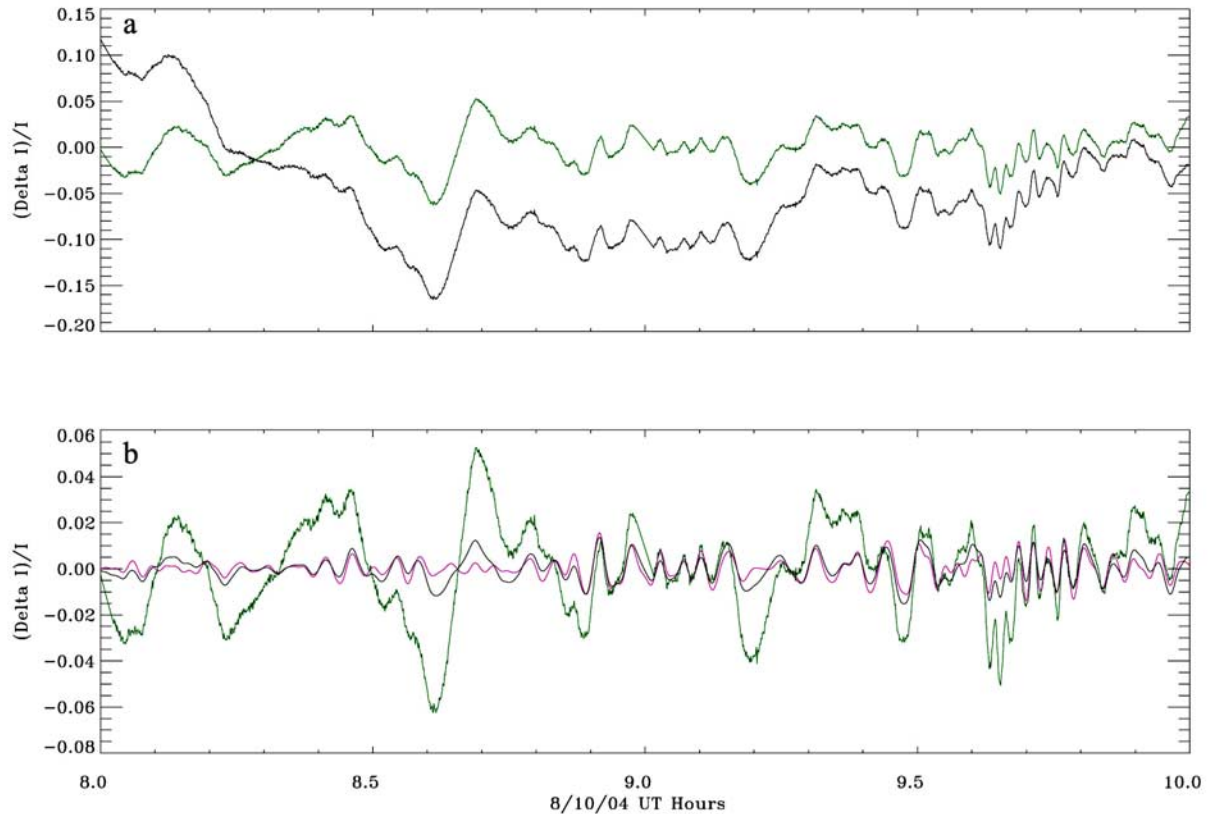
Figure 5.   (a) The black line represents the original 4-pixel smoothed time series for the period from 8 to 10 UT hours on 10 August 2004 where, as before, the mean has been subtracted (the data have been placed onto a 3-s grid) and then divided by the mean. The green line is the result when that time series is wavelet-filtered, keeping only wavelets with periods less than 20 min. (b) The green line is the same as in Figure 5a. The red line uses the DOG wavelet while the black line uses the Morlet wavelet to filter the green line plot (see text).

suited to measuring features that may be present for only a fraction of the analysis period. However, wavelet transforms are localized in frequency and in time. Thus they are excellent for measuring transient wavelike oscillations such as ripple features.

[37]   An excellent discussion of the practical series of wavelets in time series analysis is given in the paper of *Torrance and Compo* [1998]. The equations presented in that work have been coded in IDL and are available from Dr. Torrance. That software, which has been further modified by us, forms the basis for the analysis software used in this work. One wavelet, the derivative of Gaussian (DOG) discussed by *Torrance and Compo* [1998], has been selected here as the primary analysis tool. The Morlet wavelet was also considered but is more localized in frequency while the DOG is more localized in time. Except where stated, the DOG has been used.

[38]   As noted by *Torrance and Compo* [1998], wavelets provide an objective way to filter a time series since a wavelet is essentially a band-pass filter. Figure 5a shows two line plots. The black line represents the original 4-pixel smoothed time series for the period from 8 to 10 UT hours on 10 August 2004 where the data have been placed onto a

3-s grid and then divided by the mean. The resultant plot is of the fractional fluctuations. The green line is the result when that time series is wavelet-filtered, keeping only wavelets with periods less than 20 min. This is the first step in filtering in the time series.

[39]   In order to determine the occurrence frequency of ripple features, the method selected here is to simply count the number of waves over some fixed time intervals (an hour or some other observation time intervals which have periods in certain ranges). To do this, the green line plot is further filtered into three time series: one restricted to periods between 1 and 4 min, one between 4 and 8 min, and one between 8 and 20 min. An example of the first is shown in Figure 5b where the green line is the same as in Figure 5a. The red line uses the DOG while the black line uses the Morlet. Both seem to do a reasonable job of representing these period waves. Note how the small intensity noise and the longer-period waves are effectively eliminated.

[40]   Once the filtered time series are produced, the number, intensity, and period of peaks above a certain threshold are counted. The chosen threshold is 0.002. This was picked because the noise fluctuations over all frequencies are less than 0.001 based on counting statistics for the OH signal
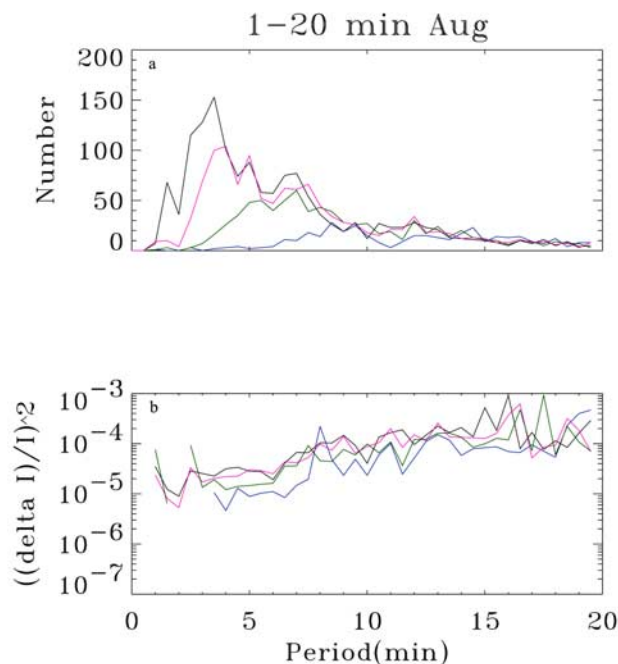
Figure 6. (a) Plots of the total number of peaks as a function of period seen in the 4 (black line), 10 (red line), 20 (green line), and 40 (blue line) pixel smoothed time series for the entire August 2004 data set. Figure 6b is same as Figure 6a but for the square of the average fractional intensity fluctuation.

retrieved from the camera for 4-pixel smoothing. The level of noise fluctuations can also be retrieved by assuming that the noise spectrum is represented by the high-frequency portion of Figure 3 and then by integrating over all frequencies to find the variance. The noise level is then derived from the square root of the variance. A threshold of 0.002 ensures a signal-to-noise ratio of at least 2. Because the band pass of the DOG in period space is wider than the chosen period limits, periods outside that range will appear. Thus, for the 1- to 4-min time series, some peaks with periods above 4 min will appear. The wider band pass of the DOG ensures that peaks in the 1- to 4-min range are not suppressed by the choice of threshold.

[41] The time series are spliced together at the boundaries, and in later sections, plots of number versus period will be shown. In addition, the average square of the fractional fluctuation will also be plotted as this shows how the different wave phenomena affect measured OH time series.

3. Results and Discussion

3.1. Observed Climatology of Wavelike Features

[42] Figure 6a shows plots of the total number of peaks as a function of period seen in the 4 (black line), 10 (red line), 20 (green line), and 40 (blue line) pixel smoothed time series for the August 2004 data set. For the 40-pixel smoothed plot, there are few peaks at periods below 6 min. Thus the periods of these waves are above the nominal Brunt-Vaisala period. Given that the horizontal wavelengths should be above approximately 20 km, or otherwise the intensities will be

greatly suppressed, these periods are consistent with the thesis referred to earlier that these are internal AGWs.

[43] While background winds clearly can shift the observed period, the lack of waves with periods below the Brunt-Vaisala period suggests that these waves may indeed be generated at altitudes well below the mesopause region, perhaps in the troposphere as has been hypothesized. The mesopause region Brunt-Vaisala period is about as low as is normally encountered [*Beer*, 1974]. In principle, waves generated at a given local altitude with an observed period below the local Brunt-Vaisala period could be internal at a particular altitude because the background wind is in a particular direction. However, between the troposphere and the mesopause region, the background winds vary considerably. Thus the wave would probably become evanescent and be greatly attenuated before it reached the mesopause.

[44] Similarly, many of the features seen in the 20-pixel smoothed plot are also consistent with those being due to AGWs. In comparison with the 40-pixel smoothed plot, the 20-pixel smoothed plot shows an increased number of peaks at periods less than 8 min. Thus this suggests that the shortest horizontal wavelength features (below 20 km) have periods less than 8 min and thus are suppressed in the 40-pixel smoothed plot. However, there are many peaks that have periods less than 5 min, and these may be due to instability or evanescent wave features.

[45] Both the 4- and 10-pixel smoothed plots show large peaks at periods less than 4 min. The number of peaks drops for periods below 3 min, with few at periods below 2 min. This is consistent with the presence of a significant number of either instabilities or evanescent waves, both of which can have periods less than 4 min. However, given that these observed features have horizontal wavelengths at or below approximately 10 km, their estimated phase speeds are well below 300 m/s, the approximate minimum value expected for internal acoustic waves. Furthermore, most of these features with short periods of less than 4 min are associated with wavelike structures that are present both over a restricted portion of the image and for a limited time period. This is very consistent, with these features being instabilities rather than evanescent waves. Thus most of the analysis that follows will assume that they are due to instabilities. However, this is not true in all cases, and an example of an evanescent wave will be discussed later.

[46] Figure 6b shows the square of the average fractional intensity fluctuation as a function of period. The instability features with below 4-min periods have lower fractional fluctuations than do have the internal AGWs. Thus they contribute to, but do not dominate in magnitude, an observed OH intensity time series.

[47] To further investigate the periods of the instability features, Figure 7a shows the difference between the 4- and 20-pixel smoothed distributions shown in Figure 6a. This effectively shows the periods of features with horizontal wavelengths below about 10 to 15 km. The black line shows the results for the August 2004 data set of Figure 6 while the blue line shows the results for the October/November 2003 data set. This clearly shows that there is a peak between 3 and 3.5 min in the distribution of these small-scale features. Taking 10 km as a nominal maximum wavelength indicates mean phase velocities of about 50 m/s or less. The 2004 data have a broader distribution of periods than does

1−20 min

1−20 min
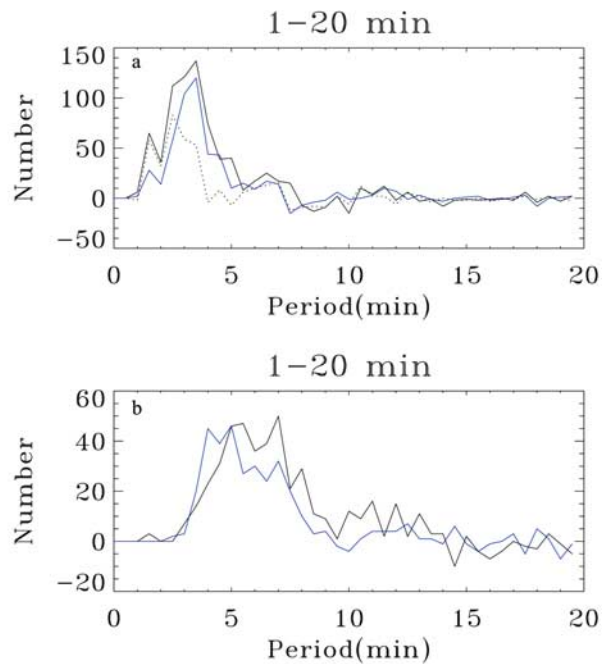
Figure 7. (a) Plots of the difference between the 4- and 20-pixel smoothed distributions. The black line shows the results for the August 2004 data set of Figure 6a while the blue line shows the results for the October/November 2003 data set. Also shown as a dotted line is the difference between the 4- and 10-pixel smoothed plots for 2004. Figure 7b is same as Figure 7a but for the difference between the 20- and 40-pixel smoothed data only.

Table 2. Smoothed Minus 20 Smoothed Results

Date	Average Period, min	Number Per Hour	Percent
16 October 2003	3.45	3.8	22
18 October 2003	2.83	6.0	28
21 October 2003	3.10	6.0	31
22 October 2003	3.32	4.0	22
23 October 2003	3.42	1.5	09
25 October 2003	3.28	4.1	22
26 October 2003	3.38	2.2	13
27 October 2003	3.83	3.0	17
28 October 2003	3.30	3.1	17
1 November 2003	3.75	3.5	22
2 November 2003	3.46	5.7	33
3 November 2003	2.93	4.7	23
4 November 2003	3.75	4.0	25
5 November 2003	3.25	5.5	30
12 November 2003	3.25	5.0	27
13 November 2003	3.00	1.0	05
15 November 2003	3.65	5.0	30
2 August 2004	3.75	2.0	13
5 August 2004	3.15	7.0	37
6 August 2004	2.83	8.7	41
7 August 2004	3.22	5.3	29
9 August 2004	3.34	2.2	12
10 August 2004	2.82	3.7	17
11 August 2004	3.11	3.0	16
12 August 2004	3.35	2.5	14
13 August 2004	3.12	3.8	20
14 August 2004	3.43	4.3	25
15 August 2004	3.24	4.6	25
16 August 2004	3.34	3.8	21
17 August 2004	2.86	3.0	14
19 August 2004	3.52	1.7	10
20 August 2004	3.19	3.4	18
21 August 2004	3.46	1.7	10
22 August 2004	3.22	3.9	21
24 August 2004	3.28	4.0	22
25 August 2004	3.75	1.8	11

have the 2003 data. Later, we will discuss a possible reason for the shape of these distributions.

[48] Also shown, as a dotted line, is the difference between the 4- and 10-pixel smoothed plots for 2004. This represents the periods for the smallest features measured in this analysis, those with wavelengths well below 10 km. The peak here occurs at 2 min, indicating that the period of the instability features scales with wavelength.

[49] Figure 7b shows similar plots for the difference between the 20- and 40-pixel smoothed data. These represent distributions of periods for the smallest-scale internal AGWs, evanescent waves, or larger-scale instability features. For the 2004 data, the peaks occur between 5 and 7 min certainly consistent with AGWs. For the 2003 data, however, the peak occurs between 4 and 5 min. Thus, in 2003, there may also be present a considerable number of either large horizontal wavelength instabilities or short horizontal wavelength AGWs. If those are AGWs, they could be either internal or evanescent.

[50] Table 2 summarizes these results by showing, for each day, the difference of the 4- and 20-pixel smoothed plots. This table shows the average apparent period and the number of peaks per hour. By multiplying these together the percent of time is derived when instabilities are seen by the imager. Table 3 shows the average results for the 2003 and 2004 data sets. These averages are quite similar, with typical periods being about 3.3 min and with features being seen for about 19% of the time. There is, however, as seen

in Table 2, considerable night-to-night variation. Also shown in Table 3 are the average results for the 20 minus 40-pixel smoothed data. The average apparent period is larger. The occurrence frequency is much less, which is only 1 to 4% of the time. Evidently, large-wavelength instabilities or short-wavelength evanescent waves are rarer.

3.2. Observations of Wavelike Features by the Lidar

[51] To further investigate the nature of these features, the analysis is restricted to the eight nights when coincident or nearly coincident lidar data are available. Figure 8 shows contour plots of Ri for each of these nights between 85 and 95 km. Regions of red (yellow) indicate where the atmosphere is convectively (dynamically) unstable based on Ri. Regions of green are where Ri is between 0.25 and 0.5. These indicate regions of possible dynamic instability, given the uncertainty in Ri, especially where green borders yellow. Note that the following discussion will focus on the 85- to 90-km region, where the bulk of the OH emission occurs.
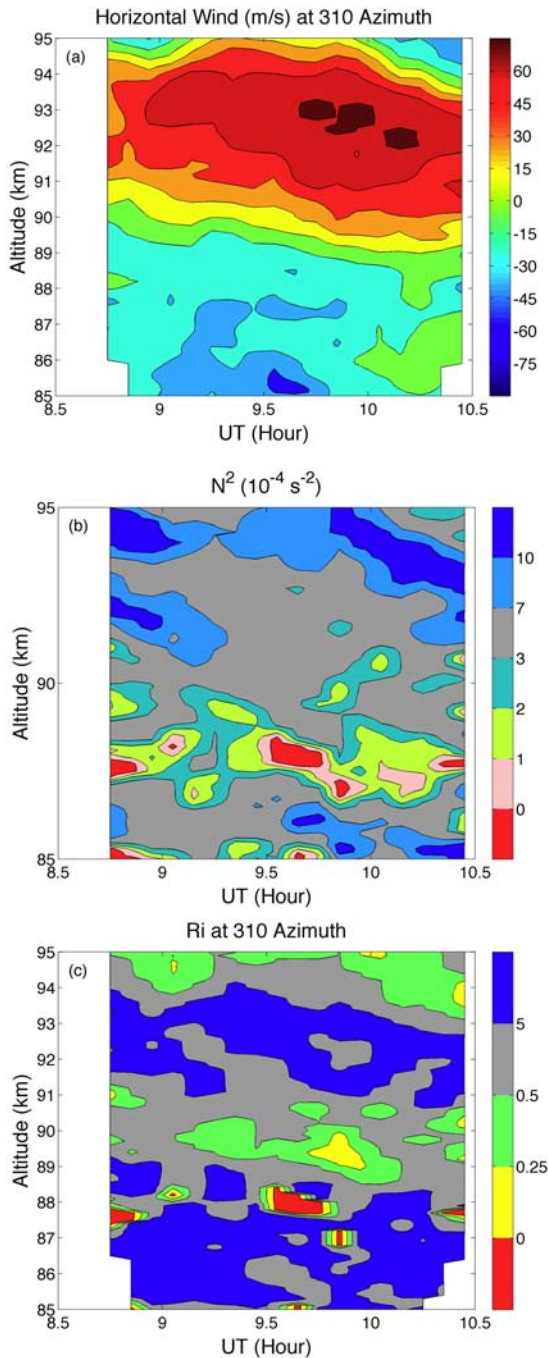
Table 3. Smoothed Minus 20 Smoothed Results

Date	Average Period, min	Number Per Hour	Percent
2003 (4 − 20)	3.31	3.52	19.4
2004 (4 − 20)	3.22	3.51	18.8
2003 (20 − 40)	3.55	0.59	3.5
2004 (20 − 40)	3.58	0.19	1.1
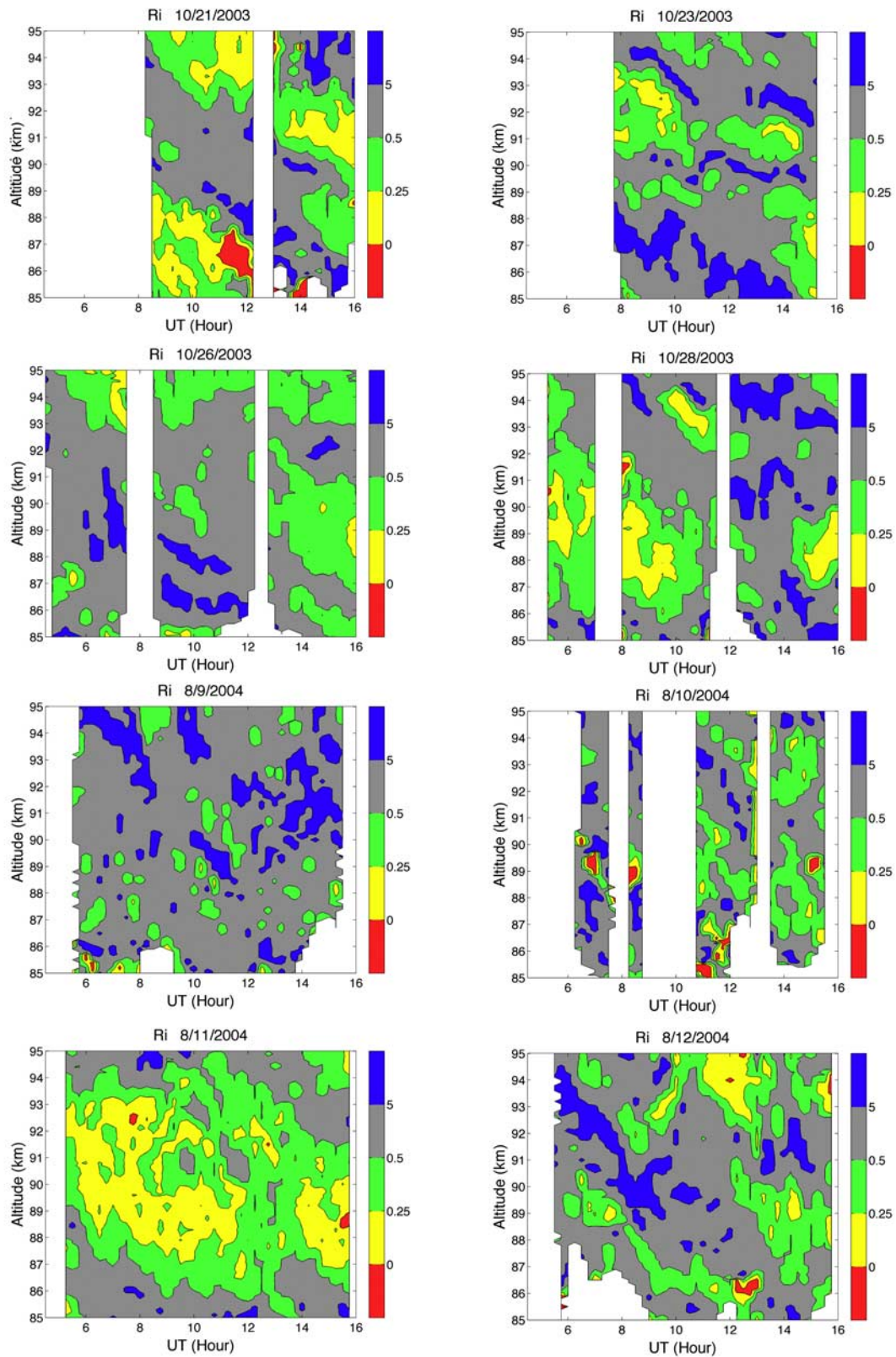
Figure 8. Eight nightly contour plots of *Ri* as determined by the lidar as a function of time and altitude.

Figure 9. Plots of lidar-derived results for the period on 10 August 2004 when the lidar was pointed toward 310° azimuth. (a) Line-of-sight wind. (b) N^2 derived from the temperature profiles. (c) A pseudo Ri derived using the results from Figures 9a and 9b.

[52] There are three nights with almost no regions of instability: 23 October 2003, 26 October 2003, and 9 October 2004. There are also three nights where there are thick (1 km or greater vertical extent) persistent regions of instability: 21 October 2003, 28 October 2003, and 11 August 2004. The convective instability seen on 10 August 2004 persists throughout most of th   t and moves toward a lower

altitude as the night progresses. This instability is reflective of a strong tide in the meridional wind present in this altitude region on that night. The downward motion of the instabilities on 21 October 2003 and 28 October 2003 is also suggestive of tidal control. As found in previous work, it appears that tides or long vertical wavelength long-period waves are very important in establishing regions of instabilities in the 85- to 90-km region [*Liu et al.*, 2004]. Nights where there are no strong tidal signatures tend to lack instability regions that are temporally persistent and vertically thick.

[53] One night, 12 August 2004, shows some periods of instability even though the atmosphere is stable during most of the night. Just around and after 12 UT hours, there was an extended period where the atmosphere had both types of instability. The night of 12 August 2003 was characterized by a strong "wall" wave as discussed by *Li et al.* [2007]. Interestingly, during the passage of the wall wave from 8 to 12 UT hours, the instabilities are suppressed. Also, during this period, the tide in the meridional wind (not shown here) appears to be absent. Around 12 UT hours, the tidal signature in the meridional wind reappears as does the presence of unstable regions around 86 km.

[54] On 10 August 2004, isolated regions of convective instability are present from 6 to 12 UT hours between 85 and 90 km. These regions also appear to descend in altitude with time reflecting perhaps a long-period wave, perhaps of tidal origin, in the temperature data. Unfortunately, there are missing data from about 8.5 to 10.5 UT hours, a period where it might be expected that the instability layers would be present in the 85- to 90-km region. The reasons for the missing data are that the lidar was pointed to a fixed azimuth of 310° during that period and that complete wind data are not available. While these data at the fixed azimuth will be discussed in more detail later, Figure 9 shows the results for the measured line-of-sight wind, N^2, and a pseudo Ri calculated using those N^2 and wind data. It can be seen that between 8.5 and 10 UT, there were indeed several predominantly convective instability regions present from 85 to 90 km.

[55] Table 4 lists for each night the percentages of either dynamically or convectively unstable regions present between 85- and 90-km altitudes for lidar observations reported for 100-m spatial and 15-min temporal bins. As noted earlier, although the data are reported at 100-m vertical

Table 4. Lidar and Imager Results[a]

Date	R0	R25	R50	R0A5	R25A5	R50A5	Imager
21 October 2003	4.3	19.9	46.4	17	67	90	31
23 October 2003	0.0	2.4	18.1	0	7	58	09
26 October 2003	0.0	1.9	22.9	0	9	37	13
28 October 2003	0.5	16.6	44.9	2	43	54	17
9 August 2004	0.5	2.5	12.6	0	7	46	12
10 August 2004	4.7	11.9	18.1	17	41	83	17
11 August 2004	0.4	29.1	22.9	2	63	21	16
12 August 2004	1.3	6.8	44.9	7	29	54	14

[a]R0 represents the percentage of time that $Ri < 0$ based on lidar data for 15-min temporal bins and 100-m spatial bins. R0A5 is the same but at 15-min resolution and anywhere between 85 and 90 km where at least 5 consecutive spatial points are less than 0. The other columns are the same but for $Ri < 0.25$ and $Ri < 0.5$. The last column show the Percent Imager results from Table 2.

bins, the effective resolution is 500 m. The columns marked with R0, R25, and R50 represent the percentage of the time the data points for Ri are less than 0, 0.25, and 0.50, respectively. The columns marked with R0A5, R25A5, and R50A5 differ in that they represent the percentage of the time when at least five consecutive spatial bins that satisfy the indicated relation are present anywhere between 85 and 90 km. The last column lists the percentage of imager ripple occurrences taken from the last column in Table 2.

[56]   The first three columns of Table 4 analyze the lidar data consistent with the study by taken by *Li et al.* [2005c] which included the 2003 data. The data suggest that for this period, at least a convective instability should be much rarer than the dynamical instability similar to what was found by *Li et al.* [2005c] when they looked at the entire 85- to 100-km region. Only two of the nights showed significant convective instability periods, 21 October 2003 and 10 August 2004. The traditional Ri cutoff of 0.25, which presumably separates unstable regions from stable regions, indicates instability probabilities of less than 30%, while if a cutoff of 0.5 is chosen, over half of the nights have a probability of over 30% of having instability regions.

3.3.   Comparisons of Lidar and Imager Observations of Wavelike Features

[57]   Before comparing these results, recall that in some sense, the two instruments are measuring different phenomena. The lidar measures whether the atmosphere is unstable. The imager is measuring the probability of observing a coherent instability feature. On the basis of the results of *Hecht et al.* [2005], the atmosphere can still be unstable after a dynamic instability feature has decayed into turbulence. In addition, the atmosphere could be stable, and a feature from a nearby region could be blown into the imager field of view. So there might not be strictly a one-to-one correspondence between the two measurements.

[58]   In addition to the three Ri results discussed above, three additional columns R0A5, R25A5, and R50A5 are also included in Table 4. Since the imager data are sensitive to instabilities anywhere in the OH emission column, the probability for an instability in the imager should be higher than was calculated in the R0, R25, and R50 columns.

[59]   The RXA5 (where X represents 0, 25, or 50) results are considerably larger than the corresponding RX results. Assuming a nominal OH emission peak near 87 km with a layer full width at half-maximum of about 10 km [e.g, *Hecht et al.*, 1998], the RXA5 data may be more representative of the instability for OH airglow images than the RX data. However, note that as an instability occurs away from the peak of the emission, it takes a larger instability density fluctuation to produce an equal fluctuation in the column OH intensity. Since the vertical extent of the unstable region is on the order of 1 km, the perturbation of the OH layer by ripples is small to begin with. Therefore ripples which occur away from the peak altitude of the OH emission are harder to observe. Thus the RX results may underestimate the probability of observing an instability in the OH emission column while the RXA5 results may be an overestimate.

[60]   First, consider the data for 2004 using the lidar R25 results. Both the lidar and imager data sets suggest that 9 and 12 August are the most stable nights while 10 and 11 August

are considerably more unstable. When the R25A5 lidar results are considered, the instability percentages increase by factors of 3 to 4 but the ranking of the nights from most to least stable does not change. In contrast, the imager data are not that much different night to night, and interestingly, all are more stable than the mean for August 2004. However, the imager data do show, as was found in the lidar data, that 9 August is more stable than 10 and 11 August, and the stability on 12 August is between that of 9 and 10 August.

[61]   For 2003, there is somewhat more consistency. From both the lidar and the imager data, the nights of 23 and 26 October are fairly stable, while those of 21 and 28 October are more unstable.

[62]   Thus the lidar and imager results are qualitatively consistent, in that nights where the atmosphere is stable tend to have the fewest instability features. It should also be noted that the qualitative agreement disappears when the R50A5 data are compared to the imager data. This suggests that at least for these data, the $Ri < 0.25$ criterion for determining an unstable region is supported. There are, however, certainly times where the lidar suggests the presence of instabilities but features are not observed.

[63]   While there is qualitative agreement, the quantitative agreement is less satisfactory. None of the lidar data columns agrees with the imager data. The biggest discrepancy is the spread between the more and less stable nights. That spread is large in the lidar data and is small in the imager data. There are also differences in the magnitude of the probabilities. The imager results for the least stable nights are lower than the lidar R25A5 results. Some of these discrepancies may be due to the fact that the OH emission sometimes occurs below 85 km, a region where the lidar is sometimes not very sensitive due to the vertical distribution of the Na layer.

[64]   There is one other nightly comparison that can be made. The lidar data suggest that convective instabilities occur predominantly on 10 August compared to the periods of 9, 11, and 12 August. Earlier studies have shown that observations of convective instabilities produce ripple features that are aligned perpendicular to AGWs [*Fritts et al.*, 1997; *Hecht et al.*, 1997, 2000]. On an image-by-image basis, there are four times as many observations of perpendicular ripple features on 10 August than on the other three nights. This is consistent with the lidar results.

[65]   To study the relationship between the imager and lidar results in more detail Figure 10 indicates the periods where the imager shows the presence of instability features. (For clarity plus signs are used to note the time when the ripples are seen. However, the width of the plus sign is not related to the extent of time when the ripple is observed.) In previous studies where isolated large horizontal wavelength ripples were observed, coincident lidar data supported the presence of unstable regions [*Hecht et al.*, 1997, 2005; *Li et al.*, 2005a, 2005b]. In the current study, in general, the periods where the lidar suggests instabilities correspond to periods where the imager is seeing features. The night of 9 August shows few instabilities compared with the night of 11 August. When instabilities do occur on 9 August, the lidar data in Figure 8 do show some regions of yellow patches indicating a dynamically unstable region. Even on 26 October, a night when the fractional amount of time the
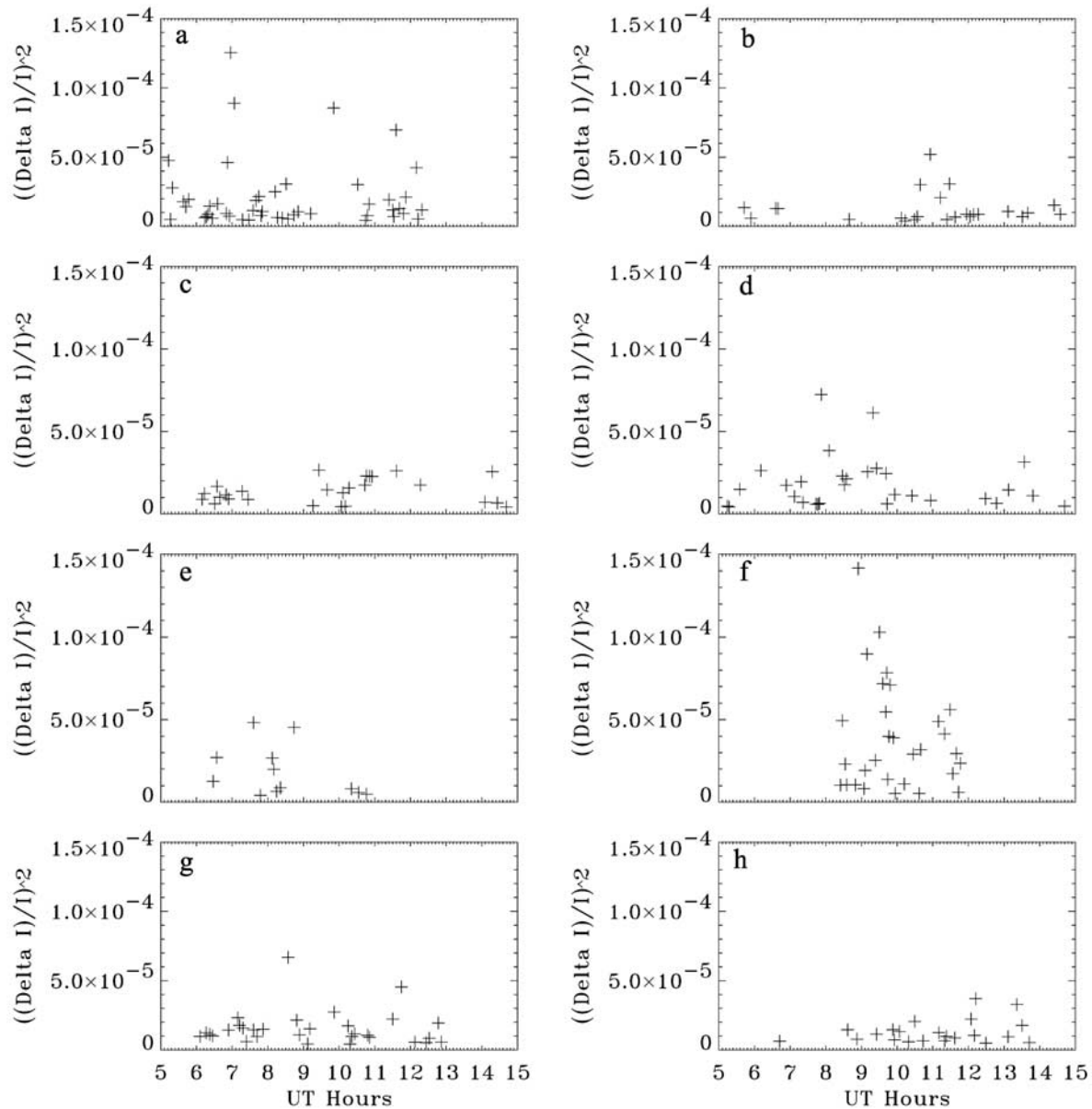
Figure 10. Plots of the square of the fractional fluctuation of individual events observed by the imager on the nights when the lidar was operating. (a) 21 October 2003. (b). 23 October 2003. (c) 26 October 2003. (d) 28 October 2003. (e) 9 August 2004. (f) 10 August 2004. (g) 11 August 2004. (h) 12 August 2004.

imager sees ripples is low, the lidar data show a considerable number of yellow patches which correspond in time to periods where the imager sees ripples.

[66] However, there are notable exceptions where there is simply no correspondence between the lidar and imager results. For example, on 21 October 2003, the atmosphere is unstable almost continuously, yet between 9 and 10 UT hours, the imager sees few features. This is probably due to the following effect also noted above. After the dynamic features form and collapse into turbulence the atmosphere may continue to be unstable. However, it is not well understood whether new instability features will continue to form.

[67] On another occasion, our method for determining the presence of ripples ma account for some of the differ-

ences. On 23 October 2003, there are features present around 10.5 UT hours when the lidar suggests a stable atmosphere. Examination of the images reveals ripple features being blown by the wind parallel to their wavefronts. While the separation of the wavefronts is about 4 km and thus is resolvable, the patchiness of these features results in an apparent observation of several short-period peaks while the images suggest one patch of multiwavefront ripples. Thus the counting procedure somewhat overestimates the frequency of instability. The lidar, however, overestimates the stability of the atmosphere since a 4-km ripple suggests an unstable layer on the order of or less than 0.5 km [e.g., *Hecht et al.*, 2005], just at the limit of the lidar resolution.

[68] While as noted below some of the short-period features identified by this method are not instabilities but
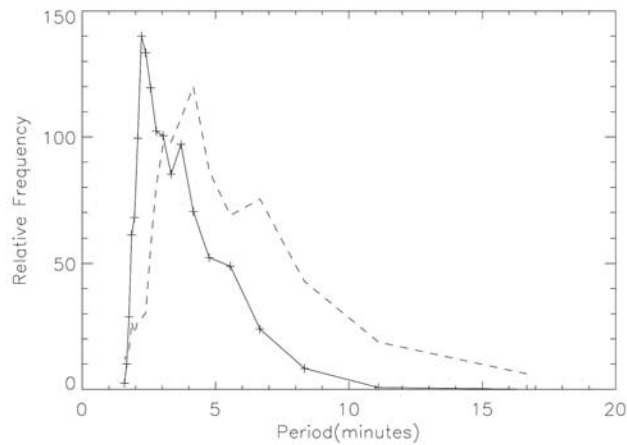
Figure 11. Histograms of the apparent period for an assumed 10-km horizontal wavelength ripple blown by the background wind. These are calculated from the measured absolute wind velocity between 85 and 90 km for the four nights in 2004 and for the four nights in 2003 where the lidar data are available (see text). Solid line is for 2004 while dashed line is for 2003.

are actually evanescent waves, examination of the images indicates that those waves are rare compared to the ripple instabilities. The evanescent wave features typically show large fractional fluctuations such as are found between 9 and 10 UT hours on 10 August 2004.

[69] To summarize, the imager data suggest that instabilities are rather frequent, occurring for about 20% of the time in the 85- to 90-km region. The lidar data complement these results by providing a limit, at the lidar vertical resolution, to the instability of the atmosphere. Even if well-defined instabilities are not observed, the atmosphere may still be turbulent.

3.4. The Distribution of the Apparent Periods of the Ripples

[70] Given that most of the features below 15-km horizontal wavelength are due to instabilities, there is a natural explanation for the shape of the plots in Figure 7. In Figure 7, the most common period occurs near 3 min; the number falls off to near 0 at 1.5 min and falls off more slowly toward longer periods. By comparing the fractional fluctuations seen in the 4- and 10-pixel smoothed plots, an estimate can be made of the horizontal wavelength of those features. For example, on 11 August 2004, a night where almost all of the features appear to be ripples, the mean wavelength is estimated to be about 10 km. This nominal wavelength is also true on most other nights when one excludes results above 15 km, which may be due to evanescent waves.

[71] Since a 10-km feature is much larger than the size of a 4-pixel box, the approximate apparent period of such a feature can be calculated by dividing 10 km by the magnitude of the wind blowing it across the box. Figure 11 shows a histogram of all periods derived from the wind between 85 and 90 km for the four total nights each in 2003 and 2004 where the lidar data are available. These histograms are normalized so that the peak is the same value as the peak number for the 4 minus   el smoothed plot of Figure 7a.

The similarity of these plots, which all have peaks below 4 min, gives support to the thesis that most of the features are indeed instabilities being blown across the field of view.
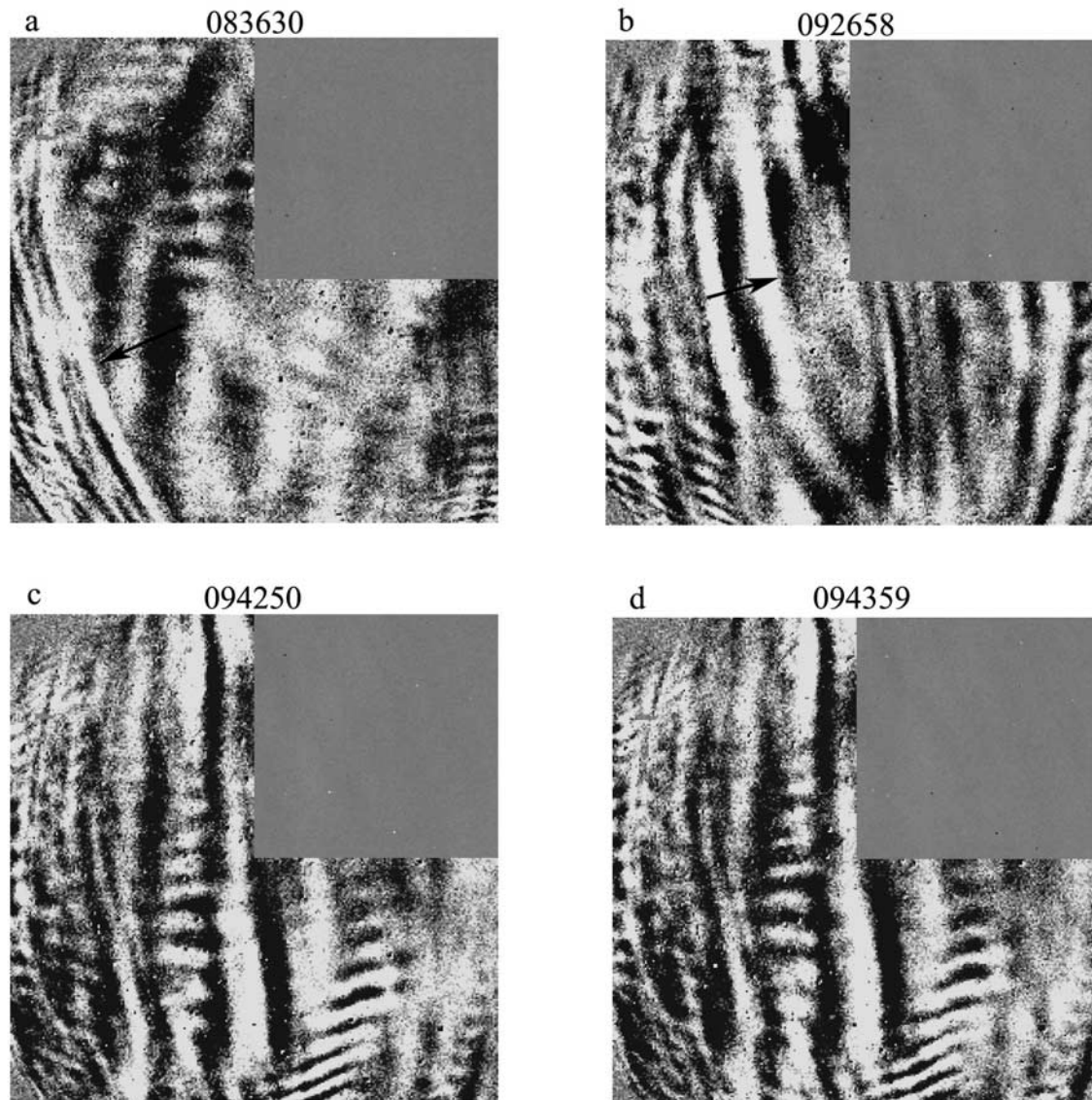
3.5. The Evanescent Wave of 10 August 2004

[72] As mentioned previously, not all of the short-period features seem to be consistent with ripple structures. An examination of Figure 10 shows that the largest fractional fluctuations observed occurred between 8.5 and 10 UT hours on 10 August 2004. This was in fact the period when the lidar was pointed toward 310° azimuth, a direction where winds can be obtained in either the 310° or 130° azimuth. This special pointing was done because the real-time observations from an all-sky airglow imager indicated the passage of a strong wavelike feature across the entire field of view, and the lidar was pointed to be perpendicular to the wavefront to measure the horizontal wind in the direction of wave propagation. This suggests that instabilities may not be the cause of all the features seen during that period.

[73] Figure 12 shows difference images for four periods between 0836 (8 hours, 36 min) and 0944 UT on 10 August 2004. In Figure 12a, the arrow points to the beginning of the wavefront which is moving from the lower left corner toward the right. In Figure 12b, at 0927 UT, the waves have completely crossed the entire frame. The arrow points across two wavefronts and is in the direction of motion which is about 120° azimuth. The separation of the wavefronts is between 13 and 15 km, and they are moving about 60 m/s, equivalent to an observed period of about 230 s. These features last for over an hour and stretch across the entire frame, and thus they are different from ripple features which typically occupy a fraction of the frame and last a few tens of minutes. Figure 12c, in fact, shows ripple features present that are aligned perpendicular to the wavefronts and are moving perpendicular to the wave motion. The ripple phase fronts barely occupy one wavelength of the waves. The speed of ripples can be determined from comparing Figures 12c and 12d.

[74] Although lidar-derived winds were measured in only one direction, at 310° azimuth, meteor radar winds are available which can be used to compute the direction of the wave features. Figure 13 shows the winds obtained during the night from both the lidar (Figures 13a and 13b), excluding the period from 8.5 to 10 UT hours, and the meteor radar (Figures 13c and 13d) over the whole night. There is good agreement especially for the 85- to 90-km region indicating that the meteor radar winds can be used during the 8.5- to 10-UT period where the lidar data are missing. Figures 13e shows the lidar temperature data which were used to compute the N^2 results in Figure 9. Figures 13f shows the meteor radar wind data at 310° azimuth, which compare favorably in the 85- to 90-km region with the lidar winds shown in Figure 9.

[75] Since the wave direction was actually closer to 120° azimuth, and the magnitude of the wind is approaching 0 near that direction, the meteor radar winds are used to determine the wind in the direction of both the wave and the ripples. It is found that the ripple motion is consistent with the wind velocity and the direction in the 85- to 90-km altitude. These ripple features are probably due to the convective instabilities seen in the lidar results near 88 km. Interestingly, these

Figure 12. Four difference images on 10 August 2004. The indicated time is that of the first image in the difference. The second image is 1 min later. (a) 083630 (8 hours, 36 min, 30 s) UT. The arrow points to the first of the evanescent wavefronts. They are moving from left to right. (b) 092658 UT. The arrow points in the direction of motion of the wavefronts. (c) 094250 UT. The perpendicular ripple features are due to convective instabilities, and they are moving approximately perpendicular to the motion of the evanescent waves. (d) 094359 UT.

ripples are perpendicular to the wave seen in the imager, which is consistent with previous observations [*Hecht et al.*, 1997, 2000].

[76] To determine if the wave is evanescent, m^2 was computed using the meteor winds at 310°, 300°, and 295°. These data can be used to determine m^2 at those azimuths or at 130°, 120°, or 115°. Similarly, the lidar winds can be used to determine the winds in either the 310° or 130° azimuth. The lidar temperatures from Figure 13 were also used. If m^2 is greater than 0, the wave is internal, but if it is less than 0, the wave is evanescent. If it is evanescent, then a scale height can be defined as the vertical distance away from the source where the wave amplitude decreases by $1/e$. When the wave is determined to be ev   ent, this also means that the

intrinsic period can be less than the Brunt-Vaisala period but above that of an internal acoustic wave.

[77] Figure 14 shows the scale height results, from 8.75 to 10.45 UT hours for the three wave azimuths using the meteor radar winds and for the single wave azimuth using the lidar winds. The scale height is defined as

$$\left(\frac{1}{2H} - \sqrt{-m^2}\right)^{-1} \tag{3}$$

where, for this region, m^2 is less than 0. A positive (negative) scale height means that the wave amplitude is increasing (decreasing) with altitude. Because of this definition of scale
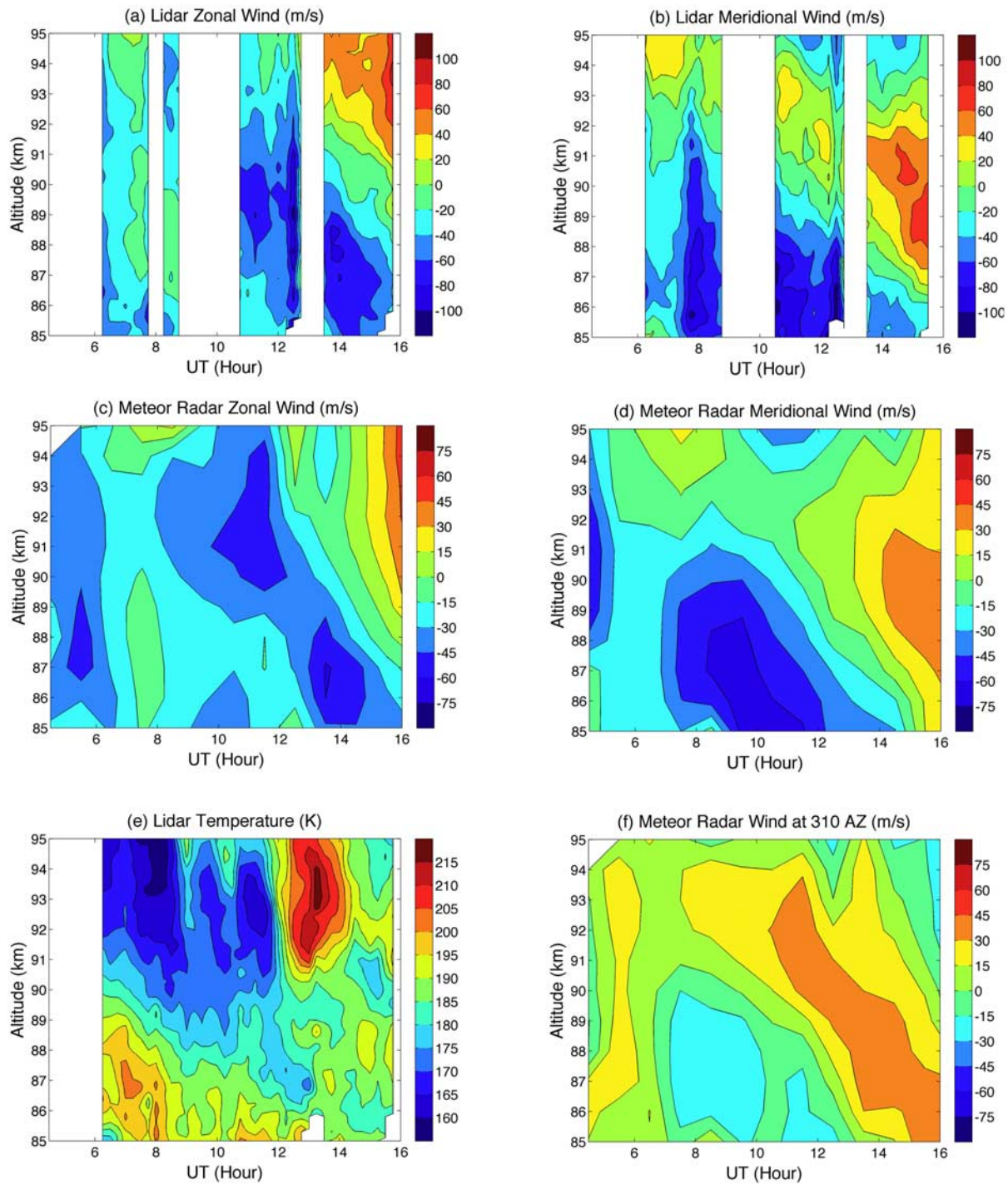
Figure 13. Data from 10 August 2004. (a) Zonal wind from the lidar. (b) Meridional wind from the lidar. (c) Zonal wind from the meteor radar. (d) Meridional wind from the meteor radar. (e) Temperature from lidar. These profiles were used to compute the N^2 shown in Figure 9b. (f) Meteor radar wind in the 310° azimuth direction derived from Figures 13c and 13d.

height, which includes the atmospheric scale height term, the evanescent region could have a positive scale height. For this example, however, the scale heights are negative. Where grey is shown, the wave is an internal AGW and is freely vertically propagating. Thus, in all cases, the wave is damped above 87 km. Note that the lid - d meteor wind-derived results are similar. In the directions close to what is measured near 0927 UT, 120° azimuth, the wave is not internal at any altitude below 90 km for the entire period. This suggests that the wave may not be observed in airglow emissions that occur predominantly above 90 km. An examination of images from the MTM in fact did not show this wave in
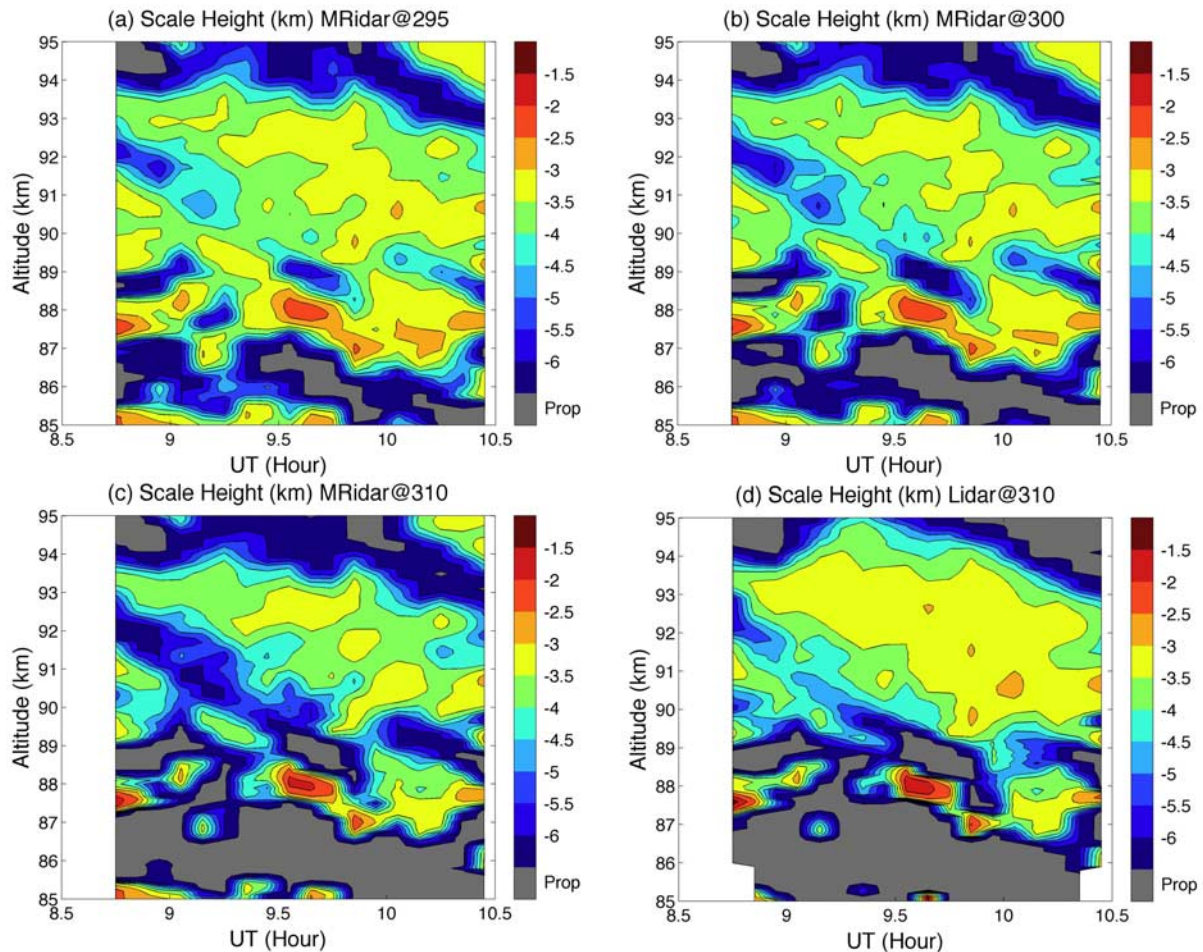
Figure 14. Scale height for the observed wave from 8.75 to 10.45 UT hours on 10 August 2004. The negative scale heights shown in color are indicative of an evanescent wave that decreases in amplitude with height. The region shown in grey is where the wave would internal and can be freely vertically propagating. This is abbreviated as prop in the color bar. The plots are derived, as indicated, from the meteor radar or the lidar winds at the indicated azimuth. (a) Meteor radar winds at 295°. (b) Meteor radar winds at 300°. (c) Meteor radar winds at 310°. (d) Lidar winds at 310°.

the O2 (0, 1) band images although it was visible in the OH (6, 2) images as would be expected from its presence in the Aerospace camera results.

[78] The wave therefore appears to be evanescent. *Walterscheid and Hecht* [2003] suggested that evanescent waves may account for some of the quasi-monochromatic waves seen in airglow imagers since evanescent waves have no vertical phase variation and thus would not be subject to cancellation effects appropriate to short vertical wavelength internal AGWs. This present example lends some support to this thesis. Certainly, when waves are seen in one airglow layer and not seen in another, this would suggest some damping and the possibility that the wave is evanescent. It is intriguing to note that for the earlier observations of convectively generated ripples, the short wavelength wave, which was not analyzed as to whether it was an internal AGW, was only seen in the OH but not in the O2 emission layer [*Hecht et al.*, 1997].

[79] The origin of such a wave is not clear. Given the temperature of about 180°, the nominal Brunt-Vaisala period, in the absence of any te   ture gradients, would be about

280 s. The observed temperature gradients would tend to increase that period. The observed period is not only well below 280 s but would almost certainly be below the nominal Brunt-Vaisala period at lower altitudes where the temperature is higher. Thus perhaps the wave was generated in situ in the 80- to 90-km altitude regime.

[80] One possibility may the parametric instability mechanism suggested by *Klostermeyer* [1990]. In that theory, a large amplitude primary gravity wave can cause a small horizontal parametric instability. This instability will have a period near the Brunt-Vaisala period and will appear to propagate similar to a wave and have little or no vertical phase variation. *Sivjee and Walterscheid* [2005] suggested this as a possible mechanism for the production of features seen, in an OH intensity time series, at observed periods of 5.6 to 5.8 min, just above the nominal Brunt-Vaisala period. For the present example, it is not clear if a large amplitude primary wave is present although, as noted earlier, the downward phase progression seen in the temperature data during this period suggests the existence of a large wave or

tide. However, whether this wave is the cause of the evanescent wave is speculative at this point.

4. Concluding Remarks and Summary

[81] The motivation for this work was the observation that time series of OH intensities taken at 3 s intervals did not show features below 4- to 5-min periods. An extensive analysis of these data showed that this occurred because those time series were binned at approximately 20×20-km horizontal distance at the nominal 85- to 90-km emission altitude of the OH Meinel band. Thus the time series was only showing fluctuations due to waves with horizontal wavelengths above 20 km, and these must be internal AGWs with periods above the Brunt-Vaisala period of approximately 5 min.

[82] However, when these same image data were binned at 2×2 km, many intensity fluctuations were seen with periods below 4 min. An examination of the full image data indicated that many of these can be associated with ripples which appear as wavelike although they only occupy a limited portion of the image.

[83] An analysis of 2 months of data from August 2004 and October/November 2003 showed that the average apparent period of the ripples was about 3.3 min and that they occur for about 20% of the time in an arbitrary but fixed 2×2-km region of the image. The nominal wavelength was about 10 km although many have wavelengths below that. Despite a considerable night-to-night variation, these averages for the two periods were about the same.

[84] The distribution of ripple periods showed that there were few at periods below 2 min, and the shape of the number-period distribution was not symmetric, with a greater number being observed at longer periods. The distribution for magnitude of the winds between 85 and 90 km was obtained from the lidar. Assuming a nominal ripple horizontal wavelength of 10 km, the distribution of periods obtained from dividing a nominal wavelength by the distribution of winds showed a similar shape to the ripple period distribution. This is consistent with the ripples being instabilities blown by the mean wind.

[85] The lidar data were examined to determine the probability of instability, and those results were compared to the probability that the imager saw a ripple feature. There was qualitative agreement in that, in general, the nights that the lidar measured to be the most stable had the fewest instabilities, and the periods when the lidar indicated that the atmosphere was unstable also corresponded to the times when the imager observed ripples. However, there was not a one-to-one correspondence; the lidar sometimes suggested an unstable region, and the imager saw no ripples and vice versa. This is perhaps not surprising as the lidar data only indicate the potential that the atmosphere is unstable while the imager data only show the presence of coherent instability features, not the subsequent turbulence. The lidar and OH imager data also do not precisely overlap in vertical extent as some of the OH emissions can occur at altitudes below 85 km where the lidar is less sensitive. It will be interesting to see if this relationship persists when a more extensive database of image and lidar data is available.

[86] While the vast majority of the features with periods around or less than 4   appear to be consistent with

instabilities, some interesting wavelike features were observed on 10 August 2004. These features, unlike ripples, occupied the full field of view. An analysis indicated that the vertical wave number was imaginary throughout most of the 85- to 90-km region, consistent with an evanescent wave. Such a wave would have no vertical phase progression and would be suppressed at higher altitudes. Indeed, these features were not observed in simultaneous O2 band emission images which typically originate above 90 km.

[87] Interestingly, at the same time, the evanescent waves were observed ripple instability structures present, whose phase fronts were perpendicular to the wave phase fronts. The ripple motion was consistent with the wind direction, and they were probably due to a convective instability observed by the lidar. The perpendicular alignment for convectively unstable ripples is consistent with observations and modeling described in earlier observations [*Hecht et al.*, 1997; *Fritts et al.*, 1997; *Hecht et al.*, 2000]. In those observations, the ripples were due to the breakdown of an identified large-scale wave and the subsequent generation of a convective instability. However, in both those observations, small-scale waves were observed to be aligned with the large-scale wave. The small horizontal wavelength of the small-scale wave meant that it was easily visible in the raw images while the large-scale wavelength was much larger than the image field of view. In the current observations, while the existence of a breaking large-scale wave is not certain, small-scale waves that aligned perpendicular to ripples are well defined.

[88] In this study, while the origin of the ripples observed on 10 August is probably due to a convective instability, the origin of the short wavelength evanescent waves is not well known. One possible explanation for their generation is the parametric instability mechanism of *Klostermeyer* [1990]. This mechanism might also explain the short wavelength waves seen in previous observations. To fully understand this, however, will require more simultaneous observations of such wave events by lidars and imagers.

[89] Finally, the data for this period do not reveal the presence of any features which have periods (generally below 3 min) and phase velocities (generally above 300 m/s) which would be consistent with the presence of internal acoustic waves. Whether this is true at other times or locations and if true why will certainly require more study.

References

Beer, T. (1974), *Atmospheric Waves*, 300 pp., John Wiley, Hoboken, N. J.
Ejiri, M. K., K. Shiokawa, T. Ogawa, K. Igarashi, T. Nakamura, and T. Tsuda (2003), Statistical study of short-period gravity waves in OH and OI nightglow images at two separated sites, *J. Geophys. Res.*, *108*(D21), 4679, doi:10.1029/2002JD002795.

Franke, S. J., X. Chu, A. Z. Liu, and W. K. Hocking (2005), Comparison of meteor radar and Na Doppler lidar measurements of winds in the mesopause region above Maui, Hawaii, *J. Geophys. Res.*, *110*, D09S02, doi:10.1029/2003JD004486.

Fritts, D. C., J. R. Isler, J. H. Hecht, and R. L. Walterscheid (1997), Wave breaking signatures in sodium densities and OH nightglow: 2. Simulation of wave and instability structures, *J. Geophys. Res.*, *102*, 6669–6684.

Gossard, E. E., and W. H. Hooke (1975), *Waves in the atmosphere, atmospheric infrasound and gravity waves—Their generation and propagation*, 456 pp., Elsevier, New York.

Hecht, J. H. (2004), Instability layers and airglow imaging, *Rev. Geophys.*, *42*, RG1001, doi:10.1029/2003RG000131.

Hecht, J. H., S. K. Ramsay Howat, R. L. Walterscheid, and J. R. Isler (1995), Observations of spectra of brightness fluctuations of the OH Meinel nightglow during ALOHA 93, *Geophys. Res. Lett.*, *22*, 2873–2876.

Hecht, J. H., R. L. Walterscheid, D. C. Fritts, J. R. Isler, D. C. Senft, C. S. Gardner, and S. J. Franke (1997), Wave breaking signatures in OH airglow and sodium densities and temperatures 1. Airglow imaging, Na lidar, and MF radar observations, *J. Geophys. Res.*, *102*, 6655–6668.

Hecht, J. H., et al. (1998), A comparison of atmospheric tides inferred from observations at the mesopause during ALOHA-93 with the model predictions of the TIME-GCM, *J. Geophys. Res.*, *103*, 6307–6322.

Hecht, J. H., C. Fricke-Begemann, R. L. Walterscheid, and J. Höffner (2000), Observations of the breakdown of an atmospheric gravity wave near the cold summer mesopause at 54°N, *Geophys. Res. Lett.*, *27*, 879–882.

Hecht, J. H., R. L. Walterscheid, and R. A. Vincent (2001), Airglow observations of dynamical (wind shear-induced) instabilities over Adelaide, Australia associated with atmospheric gravity waves, *J. Geophys. Res.*, *106*, 28,189–28,197.

Hecht, J. H., R. L. Walterscheid, M. P. Hickey, R. J. Rudy, and A. Z. Liu (2002), An observation of a fast external atmospheric acoustic-gravity wave, *J. Geophys. Res.*, *107*(D20), 4444, doi:10.1029/2001JD001438.

Hecht, J. H., S. Kovalam, P. T. May, G. Mills, R. A. Vincent, R. L. Walterscheid, and J. Woithe (2004), Airglow imager observations of atmospheric gravity waves at Alice Springs and Adelaide, Australia during the Darwin Area Wave Experiment (DAWEX), *J. Geophys. Res.*, *109*, D20S05, doi:10.1029/2004JD004697.

Hecht, J. H., A. Z. Liu, R. L. Walterscheid, and R. J. Rudy (2005), Maui Mesosphere and Lower Thermosphere (Maui MALT) observations of the evolution of Kelvin-Helmholtz billows formed near 86 km altitude, *J. Geophys. Res.*, *110*, D09S10, doi:10.1029/2003JD003908.

Klostermeyer, J. (1990), On the role of parametric instability of internal gravity waves in atmospheric radar observations, *Radio Sci.*, *25*, 983–995.

Li, F., A. Z. Liu, G. R. Swenson, J. H. Hecht, and W. A. Robinson (2005a), Observations of gravity wave breakdown into ripples associated with dynamical instabilities, *J. Geophys. Res.*, *110*, D09S11, doi:10.1029/2004JD004849.

Li, T., C. Y. She, B. P. Williams, T. Yuan, R. L. Collins, L. M. Kieffaber, and A. W. Peterson (2005b), Concurrent OH imager and sodium temperature/wind lidar observation of localized ripples over northern Colorado, *J. Geophys. Res.*, *110*, D13110, doi:10.1029/2004JD004885.

Li, Feng, A. Z. Liu, and G. R. Swenson (2005c), Characteristics of instabilities in the mesopause region over Maui, Hawaii, *J. Geophys. Res.*, *110*(D9), D09S12, doi:10.1029/2004JD005097.

Li, F., A. Liu, G. Swenson, M. Taylor, and Y. Zhao (2007), Investigation of a "wall" wave event, *J. Geophys. Res.*, *112*(D9), D04104, doi:10.1029/2006JD007213.

Liu, A. Z., R. G. Roble, J. H. Hecht, M. F. Larsen, and C. S. Gardner (2004), Unstable layers in the mesopause region observed with Na lidar during the Turbulent Oxygen Mixing Experiment (TOMEX) campaign, *J. Geophys. Res.*, *109*, D02S02, doi:10.1029/2002JD003056.

Moreels, G., and M. Herse (1977), Photographic evidence of waves around the 85 km level, *Planet. Space Sci.*, *25*, 265–273.

Nakamura, T., A. Higashikawa, T. Tsuda, and Y. Matsushita (1999), Seasonal variations of gravity wave structures in OH airglow with a CCD imager at Shigaraki, *Earth Planets Space*, *51*, 897–906.

Pautet, P.-D., M. J. Taylor, A. Z. Liu, and G. R. Swenson (2005), Climatology of short-period gravity waves observed over northern Australia during the Darwin Area Wave Experiment (DAWEX) and their dominant source regions, *J. Geophys. Res.*, *110*, D03S90, doi:10.1029/2004JD004954.

Peterson, A. W. (1979), Airglow events visible to the naked eye, *Appl. Opt.*, *18*, 3390.

Peterson, A. W., and L. M. Kieffaber (1973), Infrared photography of OH airglow structures, *Nature*, *242*, 321–322.

Sivjee, G. G., and R. L. Walterscheid (2005), Observations of elevated power near the Brunt-Väisälä frequency, *J. Geophys. Res.*, *110*, A06305, doi:10.1029/2004JA010892.

Smith, S. M., M. Mendillo, J. Baumgardner, and R. R. Clark (2000), Mesospheric gravity wave imaging at a subauroral site: First results from Millstone Hill, *J. Geophys. Res.*, *105*, 27,119–27,130.

Swenson, G. R. (2005), Preface to special section on Mesospheric Dynamic and Thermodynamic Studies, *J. Geophys. Res.*, *110*, D09S01, doi:10.1029/2004JD005490.

Swenson, G. R., M. J. Taylor, P. J. Espy, C. S. Gardner, and X. Tao (1995), ALOHA-93 measurements of intrinsic gravity wave characteristics using the airborne airglow imager and ground-based Na wind/temperature lidar, *Geophys. Res. Lett.*, *22*, 2841–2844.

Taori, A., M. J. Taylor, and S. Franke (2005), Terdiurnal wave signatures in the upper mesospheric temperature and their association with the wind fields at low latitudes (20°N), *J. Geophys. Res.*, *110*, D09S06, doi:10.1029/2004JD004564.

Taylor, M. J., and M. A. Hapgood (1990), On the origin of ripple-type wave structure in the OH airglow emission, *Planet. Space Sci.*, *38*, 1421–1430.

Taylor, M. J., and M. J. Hill (1991), Near infrared imaging of hydroxyl wave structure over an ocean site at low latitudes, *Geophys. Res. Lett.*, *18*, 1333–1336.

Taylor, M. J., M. B. Bishop, and V. Taylor (1995), All-sky measurements of short period gravity waves imaged in the OI (557.7 nm), Na (589.2 nm) and near infrared OH and O2 (0,1) nightglow emissions during the ALOHA-93 campaign, *Geophys. Res. Lett.*, *22*, 2833–2836.

Taylor, M. J., W. R. Pendleton Jr., S. Clark, H. Takahashi, D. Gobbi, and R. A. Goldberg (1997), Image measurements of short-period gravity waves at equatorial latitudes, *J. Geophys. Res.*, *102*, 26,283–26,299.

Torrance, C. T., and G. P. Compo (1998), A practical guide to wavelet analysis, *Bull. Am. Meteorol. Soc.*, *71*, 61–78.

Walterscheid, R. L., and J. H. Hecht (2003), A reexamination of evanescent acoustic-gravity waves: Special properties and aeronomical significance, *J. Geophys. Res.*, *108*(D11), 4340, doi:10.1029/2002JD002421.

————————————

S. J. Franke and A. Z. Liu, Department of Electrical and Computer Engineering, University of Illinois, 1308 W. Main Street, Urbana, IL 61801, USA. (liuzr@uiuc.edu)

J. H. Hecht, R. J. Rudy, and R. L. Walterscheid, Space Science Applications Laboratory, The Aerospace Corporation, M2-259, P. O. Box 92957, Los Angeles, CA 90009, USA. (james.hecht@aero.org; richard.rudy@aero.org; richard.walterscheid@aero.org)

P.-D. Pautet and M. J. Taylor, Center for Atmospheric and Space Sciences, Utah State University, Logan, UT 84341, USA. (mtaylor@cc.usu.edu)